Z^RZ^S males and Z^R would continue to increase in frequency, because it is selected for as a recessive in males. Third, all commercially available products in Europe contain the same CpGV isolate, which has high genetic homogeneity (*13*). Because organic apple growers rely heavily on CpGV and apply it repeatedly in each growing season, most of the organic orchards are continuously exposed to this virus isolate. Moreover, each OB of CpGV contains a single virion, in contrast to nucleopolyhedroviruses with up to several hundred virions per OB (*14*). The potential resistance-delaying effect of a mixture of virus genotypes in a single infection would thus be much weaker for CpGV.

The aim of insecticide-resistance management is to prevent or delay the selection of resistance by controlling the factors affecting allele frequencies in field populations. Our results make clear that this area of applied evolutionary biology is also highly relevant to the application of baculoviruses as biological control agents. Implementation of resistance monitoring and resistance management will be needed in order to sustain the ecological and economic benefits of this environmentally friendly class of biological insecticides.

References and Notes

1. D. Mota-Sanchez, P. S. Bills, M. E. Whalon, in *Pesticides in Agriculture and the Environment*, W. B. Wheeler, Ed. (Dekker, New York, 2002), pp. 241–272.
2. J. Mallet, *Trends Ecol. Evol.* **4**, 336 (1989).
3. F. Moscardi, *Annu. Rev. Entomol.* **44**, 257 (1999).
4. D. T. Briese, in *The Biology of Baculoviruses*, vol. 2, *Practical Application for Insect Control*, R. R. Granados, B. A. Federici, Eds. (CRC Press, Boca Raton, FL, 1986), pp. 237–263.
5. J. R. Fuxa, in *Parasites and Pathogens of Insects*, vol. 2, *Pathogens*, N. Beckage, S. Thompson, B. Federici, Eds. (Academic Press, San Diego, CA, 1993), pp. 197–209.
6. F. R. Hunter-Fujita, P. E. Entwistle, H. F. Evans, N. E. Crook, Eds., *Insect Viruses and Pest Management* (Wiley, New York, 1998).
7. E. Fritsch, K. Undorf-Spahn, J. Kienzle, C. P. W. Zebitz, J. Huber, *Nachrichtenbl. Deut. Pflanzenschutzd.* **57**, 29 (2005).
8. B. Sauphanor *et al.*, *Phytoma Déf. Vég.* **590**, 24 (2006).
9. Y. Tanada, *J. Insect Pathol.* **6**, 378 (1964).
10. J. Huber, *Mitt. Dtsch. Ges. Allg. Angew. Entomol.* **2**, 141 (1981).
11. K. E. Eberle, J. A. Jehle, *J. Invertebr. Pathol.* **93**, 201 (2006).
12. I. Fuková, P. Nguyen, F. Marec, *Genome* **48**, 1083 (2005).
13. N. E. Crook, J. D. James, I. R. L. Smith, D. Winstanley, *J. Gen. Virol.* **78**, 965 (1997).
14. D. A. Theilmann *et al.*, in *Virus Taxonomy: The Eighth Report of the International Committee on Taxonomy of Viruses*, C. M. Fauquet, M. A. Mayo, J. Maniloff, U. Desselberger, L. A. Ball, Eds. (Elsevier–Academic Press, New York, 2005), pp. 177–185.

15. We thank B. Wahl-Ermel, A. Wilhelmy, U. Poh, and E. Gabres for excellent technical assistance in insect rearing. G. Schöfl, A. Groot, A. Papanicolaou, and I. Fuková are acknowledged for advice and assistance on the larval sex-determination methods. This work was supported by a grant of the Federal Organic Farming Scheme (05OE023/1) by the Federal Agency for Agriculture and Food (BLE) of Germany, and by the Max-Planck-Society.

Supporting Online Material

www.sciencemag.org/cgi/content/full/317/5846/1916/DC1
Methods and Materials
Tables S1 and S2
References

15 June 2007; accepted 20 August 2007
10.1126/science.1146542

Transcranial Magnetic Stimulation Elicits Coupled Neural and Hemodynamic Consequences

Elena A. Allen,* Brian N. Pasley,* Thang Duong, Ralph D. Freeman†

Transcranial magnetic stimulation (TMS) is an increasingly common technique used to selectively modify neural processing. However, application of TMS is limited by uncertainty concerning its physiological effects. We applied TMS to the cat visual cortex and evaluated the neural and hemodynamic consequences. Short TMS pulse trains elicited initial activation (~1 minute) and prolonged suppression (5 to 10 minutes) of neural responses. Furthermore, TMS disrupted the temporal structure of activity by altering phase relationships between neural signals. Despite the complexity of this response, neural changes were faithfully reflected in hemodynamic signals; quantitative coupling was present over a range of stimulation parameters. These results demonstrate long-lasting neural responses to TMS and support the use of hemodynamic-based neuroimaging to effectively monitor these changes over time.

The study of brain function makes use of various techniques to modify neural processing. These include neurophysiological, surgical, and pharmacological approaches (*1*). In general, these techniques may be invasive, irreversible, and not confined to specific brain areas. In contrast, transcranial magnetic stimulation (TMS) (*2*) provides a noninvasive, reversible, and relatively localized approach that has substantial promise for basic neuroscience and clinical applications (*3*, *4*). In this technique, a magnetic coil placed above the scalp generates electric currents in the underlying cortex. As yet, the manner in which these currents affect neuronal processing is largely undetermined (*3*, *5*).

The full potential of TMS depends not only on a basic understanding of its neural effects, but also on the ability to make direct measurements of these changes in the human brain. This has recently been attempted by combining TMS with noninvasive brain-imaging techniques such as functional magnetic resonance imaging (fMRI) and positron emission tomography (PET) (*6*). These methods measure hemodynamics and metabolism to infer changes in neural activity based on known coupling between these variables (*7*). However, in certain conditions, neural activity may be uncoupled from local hemodynamics. For example, altered brain states such as seizures (*8*) and cortical spreading depression (*9*) result in complex and atypical physiological responses that do not fit standard models of neurovascular coupling. It is essential, therefore, to investigate both the direct neural effects of TMS and the relationships among neural, vascular, and metabolic parameters.

To provide an integrated view of the basic effects of TMS, we used several complementary techniques in a controlled physiological preparation. We applied short TMS pulse trains to the visual cortex of the anesthetized cat ($n = 8$) while simultaneously measuring tissue oxygen and neural activity (*10*–*12*). In separate experiments, we used 570-nm optical imaging of intrinsic signals to measure changes in total hemoglobin (Hbt) within the cortical vasculature (*12*–*14*). Each trial in our experimental paradigm (Fig. 1) included a pre-TMS baseline (40 s), a short TMS pulse train (1 to 4 s, 1 to 8 Hz), and a long recovery period (5 to 15 min). Throughout the trial, we alternated visual stimulation with a blank screen to assess the effects of TMS on both evoked and ongoing spontaneous activity (*12*). Elevation of spike rates during visual stimulation also permitted detection of signal decreases (*12*, *15*).

The neural effects of TMS application are shown in Fig. 2, A and B. An initial repeated-measures analysis of variance (ANOVA) on firing rate indicated significant main effects for activity state (spontaneous versus evoked, $F_{241,484} = 65.073$, $P < 10^{-13}$) and time (1 to 20 s after TMS, 30 to 90 s, or 180 to 210 s, $F_{241,484} = 3.473$, $P < 0.05$), as well as a significant interaction between these factors ($F_{241,484} = 9.931$, $P < 0.0001$) (*12*). Accordingly, post hoc tests (Wilcoxon signed-rank) revealed differential response time courses between activity states. Across the population, the spontaneous spike rate increased substantially (~200%) immediately after TMS (Fig. 2A, left) and remained elevated for ~60 s ($P < 0.001$; fig.

Helen Wills Neuroscience Institute, Group in Vision Science, School of Optometry, University of California, Berkeley, CA 94720, USA.

*These authors contributed equally to this work.
†To whom correspondence should be addressed. E-mail: freeman@neurovision.berkeley.edu

S4A; fig. S5A, left). In contrast, the evoked firing rate (Fig. 2A, right) showed an immediate decrease (~50%) and remained significantly suppressed for more than 5 min ($P < 0.0001$; fig. S4B; fig. S5A, middle). Analogous changes occurred in the power of local field potentials (LFPs) (Fig. 2B), although a distinction was evident with regard to frequency band (fig. S5B). Spontaneous LFP power at higher frequencies (>40 Hz) showed immediate enhancement, whereas lower frequencies (<40 Hz) exhibited a prolonged reduction, similar to evoked activity. This distinction is likely related to the different physiological processes reflected by these frequency ranges (*12*, *16*).

To determine how neural changes are reflected in metabolic and vascular signals, we examined measurements of tissue oxygen colocalized with the neural recordings. A repeated-measures ANOVA showed a significant main effect for time ($F_{111,224} = 56.609$, $P < 10^{-16}$) but no effect for activity state ($F_{111,224} = 0.0001$, $P > 0.98$; fig. S6B). Therefore, oxygen was further analyzed as a single continuous variable (*12*, *17*). Post hoc Wilcoxon signed-rank tests revealed a biphasic response pattern for oxygen (Fig. 2C). An immediate increase peaked at 10 to 15 s after TMS (Fig. 2C, inset; $P < 0.001$) and was followed by an extended reduction lasting over 2 min ($P < 0.01$). Separate measurements of Hbt (Fig. 2D) revealed a similar response: a peak at 10 s (Fig. 2D, inset; $P < 10^{-7}$) and a subsequent prolonged decrease (over 1 min, $P < 0.001$). This independent data set confirms that changes in blood flow underlie a substantial component of the oxygen response.

The above ANOVAs also revealed significant main effects of pulse frequency (1, 4, or 8 Hz) on neural ($F_{241,484} = 3.522$, $P < 0.05$) and oxygen ($F_{111,224} = 5.739$, $P < 0.005$) data. This raises the possibility that neural and hemodynamic response components covary with stimulation parameters. During the initial response component (<20 s), an increase in TMS pulse frequency caused a monotonic increase in the amplitude of the early oxygen peak and the level of spontaneous neural firing (Fig. 3A, upper right quadrant). At later time points (30 to 90 s), reductions in both tissue oxygen and evoked spiking were larger with

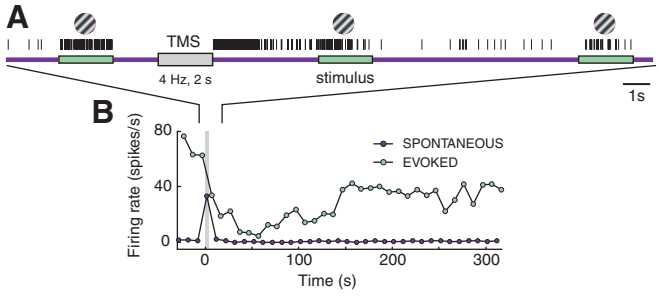

Fig. 1. TMS and visual stimulation paradigm. (**A**) Timeline of a sample trial showing stimulus presentations (green) and interstimulus intervals (ISIs) (purple). The visual stimulus was a high-contrast grating displayed for 2 s at intervals of 8 s. TMS (gray box) was applied during an ISI. TMS pulse trains were varied in frequency and duration on separate trials. Single-unit spikes (black ticks), LFP (not shown), and tissue oxygen (not shown) were recorded continuously; activity during TMS was not analyzed because of artifact contamination (fig. S3A). (**B**) The full TMS trial. Evoked activity represents neural responses during stimulus presentations, and spontaneous activity represents responses that occurred during ISIs.

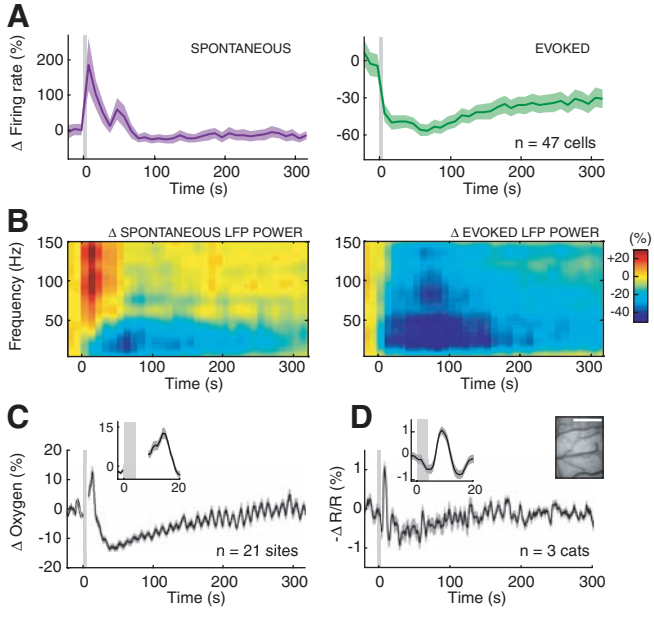

Fig. 2. Effects of TMS on neural, oxygen, and optical imaging signals. Shown are average time courses of (**A**) spiking activity, (**B**) LFP power, (**C**) tissue oxygen, and (**D**) total hemoglobin (Hbt) before and after TMS (gray box). All signals are expressed as a percent change from their pre-TMS baselines. Shaded areas represent ±1 SEM. (A) Spontaneous (left) and evoked (right) spiking activity ($n = 47$ cells). (B) Spontaneous (left) and evoked (right) LFP power ($n = 42$ sites). (C) Tissue oxygen ($n = 21$ sites). (D) Hbt ($n = 3$ animals). Insets in (C) and (D) show initial increases. Time periods containing TMS artifacts were removed (fig. S3B). In (D), Hbt was measured by recording the change in 570-nm light reflectance (ΔR/R) from the cortical surface (upper right); scale bar, 1 mm.

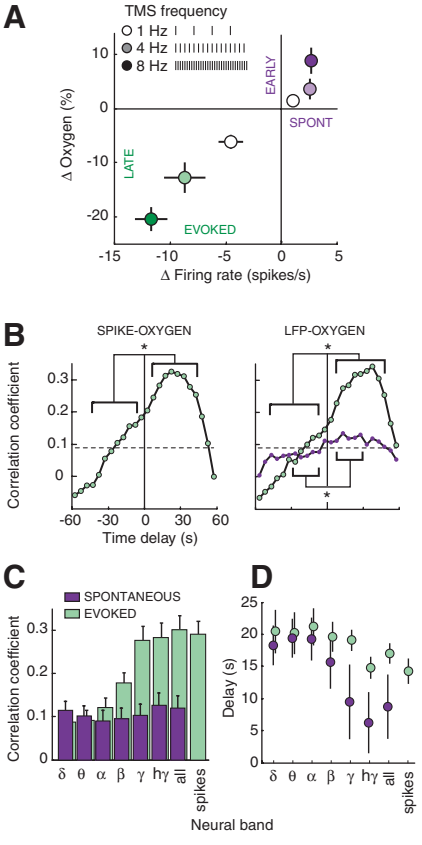

Fig. 3. Covariation between neural and oxygen data. (**A**) Changes in spiking activity and oxygen as a function of TMS pulse frequency. Neural activity was indexed by spontaneous spiking during the initial phase (0 to 20 s after TMS) and by evoked spiking during the later phase (30 to 90 s) (*15*). Error bars in this and subsequent panels represent ±1 SEM; where error bars are not visible, the error was smaller than the plot symbol. (**B**) Time-lag correlation between oxygen and neural signals (left: spiking activity, $n = 117$ trials; right: LFP power, 1 to 150 Hz, $n = 77$ trials). Positive time lags indicate a shift of the neural signal forward in time relative to the oxygen signal. Neural-oxygen correlations were performed for evoked spiking and LFP activity (green) and for spontaneous LFP signals (purple); a similar analysis with spontaneous spiking could not be performed because of low baseline firing rates. Correlation coefficients above the dashed lines are significant over the population ($P < 0.05$, t test). Asterisks denote correlations at positive time lags that are significantly greater than those at negative delays ($P < 0.05$, paired t test). (**C**) Neural-oxygen correlation magnitude across bands. LFP bands are defined as follows: δ (delta; 1 to 4 Hz), θ (theta; 4 to 8 Hz), α (alpha; 8 to 12 Hz), β (beta; 12 to 20 Hz), γ (gamma; 20 to 80 Hz), hγ (high-gamma; 80 to 150 Hz), all (1 to 150 Hz). (**D**) Neural-oxygen correlation latencies across bands.

higher pulse frequencies (Fig. 3A, lower left quadrant). A more limited data set for pulse train duration showed an analogous trend (fig. S7B). These data suggest that the physiological effects of TMS increase in a dose-dependent manner within this regime of TMS application.

The relationship between decreases in oxygen and neural activity is consistent with recent studies of negative hemodynamic responses (*18*, *19*). However, reductions in oxygen may be a cause of neural suppression rather than a consequence. In this scenario, normal neural function would be limited by hypoxic conditions (*12*). To investigate this possibility, we performed a time-lag correlation analysis of simultaneously acquired neural and oxygen data (fig. S8). Both spike rate (Fig. 3B, left) and LFP power (Fig. 3B, right) showed significant correlations with oxygen across a broad range of time lags ($P < 0.05$, t test). Notably, correlation coefficients were significantly greater at time lags in which the neural signal was shifted forward in time ($P < 0.05$, paired t test). Furthermore, LFP-oxygen correlations were band-specific with regard to magnitude and latency. Gamma and high-gamma bands exhibited the strongest correlations (Fig. 3C), as reported in previous studies of hemodynamic coupling (*20*). Higher-frequency bands also exhibited peak correlations at shorter latencies (Fig. 3D). This trend, which was most pronounced for spontaneous activity, resulted from initial response increases present in higher-frequency but not lower-frequency bands (Fig. 2B, left). These analyses, along with additional experiments (fig. S9) (*12*), suggest that oxygen responses follow neural activity in a manner consistent with neurovascular coupling (*21*–*24*).

A striking aspect of our data is the long duration of neural and hemodynamic changes given the short application of TMS. Although most human studies using similar stimulation paradigms have demonstrated short-term effects, several studies have noted changes in cortical excitability on the order of minutes (*25*, *26*). Human studies using longer-duration stimulation have shown effects lasting hours or even days (*27*, *28*). Such long-term changes in neural function are thought to develop via spike timing–dependent plasticity (*27*, *29*, *30*). Notably, alterations in synaptic efficacy have been linked to changes in the temporal relationship between spikes and LFP oscillations (*31*, *32*). To examine our data for a link between spike timing and long-term neural changes, we performed an additional analysis of phase relationships between single-unit spikes and LFP oscillations (*12*, *33*). For pre- and post-TMS time windows, we quantified the degree of phase locking from the distribution of LFP phases at which spikes occurred (Fig. 4A). A striking example of TMS-induced changes in phase distributions is shown for spontaneous activity in Fig. 4B. Compared to the pre-TMS baseline (blue), spike timing relative to the theta oscillation was strongly desynchronized, as evidenced by the increased spread of the distribution after TMS (red). Across all frequency bands, spontaneous activity showed significant reductions in phase locking within the first 30 s after TMS (Fig. 4C, left, $P < 0.05$, randomization test). By 90 s, this index approached baseline values, and in the gamma band it actually exhibited a significant increase ($P < 0.05$). Somewhat similar effects were present in evoked activity (Fig. 4C, right). Phase locking to oscillations in the delta band were strongly reduced, whereas increases were present in both the gamma and high-gamma bands ($P < 0.05$). The capacity of TMS to disrupt precise timing of signals between interconnected neurons advocates its ability to alter brain plasticity (*27*, *29*, *30*) in a number of neuropsychiatric contexts (*4*).

Consistent with previous work (*29*, *34*, *35*), our results reveal long-lasting neural and hemodynamic consequences of TMS that covary with stimulation duration and frequency. In contrast, other studies have reported a distinction whereby low-frequency stimulation (≤1 Hz) causes suppression and high-frequency stimulation (≥8 Hz) leads to facilitation (*5*). However, this division appears to be oversimplified (*5*, *36*). The precise effects of brain stimulation are fundamentally dependent on many factors (*37*). For example, several groups have found that identical TMS paradigms elicit opposite physiological effects when applied to neighboring cortical regions (*34*, *38*) or different subjects (*36*). Within a single site, TMS can produce differential effects depending on the activity state to which stimulation is paired (*36*, *39*). Such reports of variability and state-dependence reveal the complex action of TMS, yet also hint at its potential flexibility as an interventional technique.

Harnessing this potential requires the ability to measure the precise neural effects of TMS over different brain regions and time intervals. Our findings show that TMS-induced modifications of neural activity are readily observed in cerebral hemodynamics, which can be detected by standard neuroimaging techniques. This result confirms recent combined TMS-fMRI studies in which correlations were reported between TMS-induced behavioral changes and hemodynamic signals in functionally related brain regions (*39*, *40*). The capacity of brain imaging to monitor the temporal progression of physiological changes induced by TMS may prove highly beneficial for the development and optimization of both basic neuroscience and clinical applications.

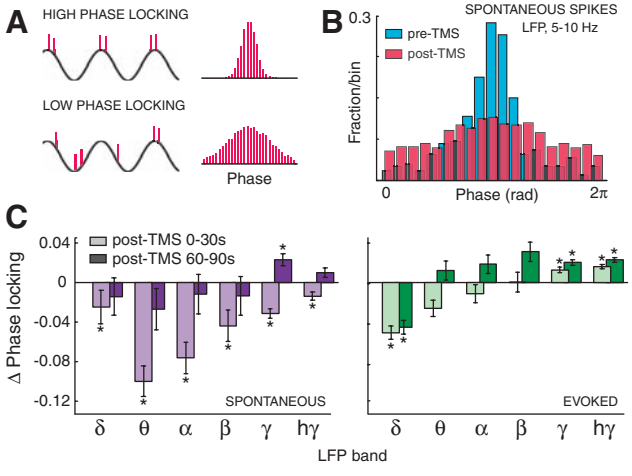

Fig. 4. Effects of TMS on spike timing relative to LFP oscillations. (**A**) Illustration of phase locking between spikes (red) and LFP (black). During periods of high phase locking (top), spikes occur at consistent phases in the LFP (left), and the resulting phase distribution is narrow (right). (**B**) Example of a TMS-induced change in phase locking. Before TMS (blue), spontaneous spikes occur more frequently at preferred phases of theta-band oscillation. In the first 30 s after TMS (red), the phase distribution broadens, indicating a decrease in phase locking. (**C**) Changes in phase locking across LFP frequency bands for spontaneous (left) and evoked (right) activity. Change in phase locking was determined by comparing the vector strengths (one minus the circular variance) of phase distributions before and after TMS. Light bars show changes in the first 30 s after TMS; dark bars show changes at 60 to 90 s. Asterisks indicate significance ($P < 0.05$, randomization test).

References and Notes

1. N. Singh, V. Pillay, Y. E. Choonara, *Prog. Neurobiol.* **81**, 29 (2007).
2. A. T. Barker, R. Jalinous, I. L. Freeston, *Lancet* **i**, 1106 (1985).
3. A. Pascual-Leone, V. Walsh, J. Rothwell, *Curr. Opin. Neurobiol.* **10**, 232 (2000).
4. M. S. George, R. H. Belmaker, *Transcranial Magnetic Stimulation in Clinical Psychiatry* (American Psychiatric Publishing, Washington, DC, ed. 1, 2007).
5. P. B. Fitzgerald, S. Fountain, Z. J. Daskalakis, *Clin. Neurophysiol.* **117**, 2584 (2006).
6. A. T. Sack, D. E. Linden, *Brain Res. Brain Res. Rev.* **43**, 41 (2003).
7. Y. Zheng *et al.*, *Neuroimage* **16**, 617 (2002).
8. M. Suh, S. Bahar, A. D. Mehta, T. H. Schwartz, *J. Neurosci.* **25**, 68 (2005).
9. T. Takano *et al.*, *Nat. Neurosci.* **10**, 754 (2007).
10. J. K. Thompson, M. R. Peterson, R. D. Freeman, *Science* **299**, 1070 (2003).
11. The partial pressure of oxygen within extravascular tissue is sensitive to changes in both cerebral blood flow and the rate of oxidative metabolism (*10*).
12. See supporting material on *Science* Online.
13. Hbt is quantitatively related to cerebral blood flow (*14*) and therefore provides an independent measurement of this variable.
14. R. L. Grubb Jr., M. E. Raichle, J. O. Eichling, M. M. Ter-Pogossian, *Stroke* **5**, 630 (1974).
15. During suppressive phases, we use evoked rather than spontaneous spiking to index neural activity because

baseline spontaneous activity (~1 spike/s) is typically too low to detect signal decreases.
16. A. von Stein, J. Sarnthein, *Int. J. Psychophysiol.* **38**, 301 (2000).
17. One might expect to observe visually elicited oxygen responses during the evoked intervals of the TMS trial (fig. S2B). However, stimulus-evoked responses are considerably smaller and more variable than TMS-induced oxygen responses, and are therefore negligible in the current paradigm (fig. S6).
18. A. Shmuel, M. Augath, A. Oeltermann, N. K. Logothetis, *Nat. Neurosci.* **9**, 569 (2006).
19. B. N. Pasley, B. A. Inglis, R. D. Freeman, *Neuroimage* **36**, 269 (2007).
20. J. Niessing *et al.*, *Science* **309**, 948 (2005).
21. On the basis of previous work in awake animals (*22*) and the similarity of neurovascular organization (*23*, *24*) across the cortex, we expect that preserved coupling after TMS will generalize to a broad range of cortical regions and physiological states.
22. J. Berwick *et al.*, *J. Cereb. Blood Flow Metab.* **22**, 670 (2002).
23. C. Iadecola, *Nat. Rev. Neurosci.* **5**, 347 (2004).
24. H. M. Duvernoy, S. Delon, J. L. Vannson, *Brain Res. Bull.* **7**, 519 (1981).
25. A. Pascual-Leone, J. Valls-Sole, E. M. Wassermann, M. Hallett, *Brain* **117**, 847 (1994).
26. B. Takano *et al.*, *Neuroimage* **23**, 849 (2004).
27. Y. Z. Huang, M. J. Edwards, E. Rounis, K. P. Bhatia, J. C. Rothwell, *Neuron* **45**, 201 (2005).
28. F. Maeda, J. P. Keenan, J. M. Tormos, H. Topka, A. Pascual-Leone, *Clin. Neurophysiol.* **111**, 800 (2000).
29. H. Wang, X. Wang, H. Scheich, *Neuroreport* **7**, 521 (1996).
30. S. F. Cooke, T. V. Bliss, *Brain* **129**, 1659 (2006).
31. C. Holscher, R. Anwyl, M. J. Rowan, *J. Neurosci.* **17**, 6470 (1997).
32. V. Wespatat, F. Tennigkeit, W. Singer, *J. Neurosci.* **24**, 9067 (2004).
33. J. Jacobs, M. J. Kahana, A. D. Ekstrom, I. Fried, *J. Neurosci.* **27**, 3839 (2007).
34. T. Paus *et al.*, *J. Neurophysiol.* **79**, 1102 (1998).
35. H. R. Siebner *et al.*, *Neuroimage* **14**, 883 (2001).
36. A. Pascual-Leone *et al.*, *J. Clin. Neurophysiol.* **15**, 333 (1998).
37. M. L. Kringelbach, N. Jenkinson, S. L. Owen, T. Z. Aziz, *Nat. Rev. Neurosci.* **8**, 623 (2007).
38. A. M. Speer *et al.*, *Biol. Psychiatry* **54**, 826 (2003).
39. A. T. Sack *et al.*, *Cereb. Cortex* (2007).
40. C. C. Ruff *et al.*, *Curr. Biol.* **16**, 1479 (2006).
41. We thank our colleagues at the University of California, Berkeley, and anonymous reviewers for their helpful comments, and R. Bartholomew, N. Lines, and L. Gibson for assistance in developing the electrophysiological apparatus. Supported by research and CORE grants from the National Eye Institute (EY01175 and EY03176, respectively) and by NSF graduate research fellowship 2003014861.

Supporting Online Material
www.sciencemag.org/cgi/content/full/317/5846/1918/DC1
Materials and Methods
Figs. S1 to S9
References

13 June 2007; accepted 21 August 2007
10.1126/science.1146426

Genomic Minimalism in the Early Diverging Intestinal Parasite *Giardia lamblia*

Hilary G. Morrison,[1]* Andrew G. McArthur,[1] Frances D. Gillin,[2] Stephen B. Aley,[3] Rodney D. Adam,[4] Gary J. Olsen,[5] Aaron A. Best,[6] W. Zacheus Cande,[7] Feng Chen,[8] Michael J. Cipriano,[1] Barbara J. Davids,[2] Scott C. Dawson,[9] Heidi G. Elmendorf,[10] Adrian B. Hehl,[11] Michael E. Holder,[1] Susan M. Huse,[1] Ulandt U. Kim,[1] Erica Lasek-Nesselquist,[1] Gerard Manning,[12] Anuranjini Nigam,[4] Julie E. J. Nixon,[1] Daniel Palm,[13] Nora E. Passamaneck,[1] Anjali Prabhu,[4] Claudia I. Reich,[5] David S. Reiner,[2] John Samuelson,[14] Staffan G. Svard,[15] Mitchell L. Sogin[1]

The genome of the eukaryotic protist *Giardia lamblia*, an important human intestinal parasite, is compact in structure and content, contains few introns or mitochondrial relics, and has simplified machinery for DNA replication, transcription, RNA processing, and most metabolic pathways. Protein kinases comprise the single largest protein class and reflect *Giardia*'s requirement for a complex signal transduction network for coordinating differentiation. Lateral gene transfer from bacterial and archaeal donors has shaped *Giardia*'s genome, and previously unknown gene families, for example, cysteine-rich structural proteins, have been discovered. Unexpectedly, the genome shows little evidence of heterozygosity, supporting recent speculations that this organism is sexual. This genome sequence will not only be valuable for investigating the evolution of eukaryotes, but will also be applied to the search for new therapeutics for this parasite.

Giardia lamblia (syn. *G. intestinalis*, *G. duodenalis*) is the most prevalent parasitic protist in the United States, where its incidence may be as high as 0.7% (*1*). Worldwide, giardiasis is common among people with poor fecal-oral hygiene, and major modes of transmission include contaminated water supplies or sexual activity. Flagellated giardial trophozoites attach to epithelial cells of the small intestine, where they can cause disease without triggering a pronounced inflammatory response. There are no known virulence factors or toxins, and variable expression of surface proteins may allow evasion of host immune responses and adaptation to different host environments. Trophozoites can differentiate into infectious cysts that are transmitted through feces.

Unusual features of this enigmatic protist include the presence of two similar, transcriptionally active diploid nuclei and the absence of mitochondria and peroxisomes. *Giardia* is a member of the Diplomonadida, which includes both free-living (e.g., *Trepomonas*) and parasitic species. The phylogenetic position of diplomonads and related excavate taxa is perplexing. Ribosomal RNA (rRNA), vacuolar ATPase (adenosine triphosphatase), and elongation factor phylogenies identify *Giardia* as a basal eukaryote (*2*–*4*). Other gene trees position diplomonads as one of many eukaryotic lineages that diverged nearly simultaneously with the opisthokonts and plants. Discoveries of a mitochondrial-like *cpn60* gene and a mitosome imply that the absence of respiring mitochondria in *Giardia* may reflect adaptation to a microaerophilic life-style rather than divergence before the endosymbiosis of the mitochondrial ancestor (*5*, *6*). Because of its impact on human disease and its relevance to understanding the evolution of eukaryotes, we embarked upon a genome analysis of *G. lamblia*.

The genome of *G. lamblia* WB clone C6 (ATCC50803) is ~11.7 MB in size, distributed on five chromosomes. The edited draft genome sequence contains 306 contigs on 92 scaffolds (Supporting Online Material). The genome is compact. We identified 6470 open reading frames (ORFs) with a mean intergenic distance of 372 base pairs (bp) (Table 1). Approximately 77% of the assembled sequence defines ORFs, of which 1800 overlap and 1500 more are within 100 nucleotides (nt) of an adjacent ORF. Serial analysis of gene expression (SAGE) and cDNA sequences provided transcriptional evidence for 4787 of these ORFs (Supporting Online Material).

Although the total number of ORFs is similar to that of yeast, many specific giardial pathways appear simple in comparison with those of other eukaryotic organisms. *Giardia*'s genome encodes a simplified form of many cellular processes: fewer and more basic subunits, incorporation of single-domain bacterial- and archaeal-like en-

[1]Marine Biological Laboratory, Woods Hole, MA 02543–1015, USA. [2]Department of Pathology, Division of Infectious Diseases, University of California, San Diego, CA 92103–8416, USA. [3]Department of Biological Sciences, University of Texas at El Paso, El Paso, TX 79968–0519, USA. [4]Departments of Medicine and Immunobiology, University of Arizona College of Medicine, Tucson, AZ 85724–5049, USA. [5]Department of Microbiology, University of Illinois at Urbana-Champaign, Urbana, IL 61801, USA. [6]Department of Biology, Hope College, Holland, MI 49423, USA. [7]University of California, Berkeley, CA 94720–3200, USA. [8]University of Pennsylvania, Philadelphia, PA 19194, USA. [9]University of California, Davis, CA 95616, USA. [10]Biology Department, Georgetown University, Washington, DC 20057, USA. [11]Institute of Parasitology, University of Zürich, CH-8057 Zürich, Switzerland. [12]Razavi Newman Center for Bioinformatics, The Salk Institute for Biological Studies, La Jolla, CA 92037–1099, USA. [13]Centre for Microbiological Preparedness, Swedish Institute for Infectious Disease Control, 171 82 Solna, Sweden. [14]Department of Molecular and Cell Biology, Boston University Goldman School of Dental Medicine, Boston, MA 02118–2932, USA. [15]Department of Cell and Molecular Biology, Uppsala University, SE-751 24 Uppsala, Sweden.

*To whom correspondence should be addressed. E-mail: morrison@mbl.edu

Supporting Online Material

Materials and Methods:

A total of eight mature cats were used in this study. All procedures complied with the National Institutes of Health Guide for the Care and Use of Laboratory Animals and were approved by the Animal Care and Use Committee at the University of California Berkeley.

Surgery and Anesthesia: Surgical anesthesia was induced with isofluorane (4%). After placement of venous catheters, anesthesia was continued with intravenous infusion of fentanyl citrate (10 μg.kg^{-1}.hr^{-1}) and thiopental sodium (6.0 mg. kg^{-1}.hr^{-1}). Additional bolus injections of thiopental sodium were given as needed during surgery. Following the placement of a tracheal cannula, animals were artificially ventilated with a 25% O_2 / 75% N_2O mixture. Respiration rate was adjusted to maintain expired CO_2 between 30-36 mmHg (generally between 15-25 breaths/min). In one cat, moderate hypercapnia was induced to manipulate levels of tissue oxygen. For this procedure, 5% CO_2 was added to the inspired gas, and the fraction of N_2O was reduced to keep inspired O_2 constant. After 4.5 minutes, the gas mixture was returned to 25% O_2 / 75% N_2O. A minimum of 30 minutes was provided for recovery before beginning another period of hypercapnia. Body temperature was maintained at 38º C with a closed-loop controlled heating pad (Love Controls, IN, USA). A craniotomy was performed over area 17 (Horsley-Clarke coordinates P4, L2 (*1*)) and the dura was resected. The craniotomy was then covered with agar and wax to form a closed chamber. After completion of surgical procedures, fentanyl citrate infusion was discontinued and the rate of thiopental sodium infusion was gradually lowered to a level at which the animal was stabilized. This level of infusion was determined individually for each animal (typically 1.5 to 2.0 mg. kg^{-1}.hr^{-1}). After stabilization, the animal

was immobilized with an intravenous infusion of pancuronium bromide (0.2 $mg.kg^{-1}.hr^{-1}$) to prevent eye movements. The pupils were dilated with drops of 1% atropine sulfate, and nictitating membranes were retracted with 2.5% phenylephrine hydrochloride. Rigid contact lenses with 3 mm artificial pupils were fitted to the eyes. EEG, ECG, heart rate, temperature, end-tidal CO_2, and intra-tracheal pressure were monitored through the duration of the experiment.

***Visual Stimulation*:** Visual stimuli consisted of sinusoidal gratings presented on a luminance-calibrated CRT monitor (85 Hz refresh rate, mean luminance 45 cd/m^2). Preliminary tests were performed on each neuron to identify the stimulus orientation, spatial frequency, temporal frequency, position, and size to maximize the neuron's spike response. During TMS trials drifting gratings with optimal parameters were displayed at 50% contrast for 2 s.

TMS: TMS was applied to the cat visual cortex using a MagStim Rapid system (The MagStim Company Ltd., Whitland, UK) with a 70 mm figure-eight coil. The coil was positioned using a mechanical camera arm. For most experiments the coil was positioned posterior to the visual cortex and angled 45 degrees towards the horizontal plane, which permitted an electrode penetration into area 17 at Horsely-Clarke coordinates P3.5, L2, with an angle of P45, M0 (fig. S1A). During optical imaging experiments, the coil position was adjusted to create an unobstructed view for the macrolens. This involved reducing the angle between the face of the TMS coil and the coronal plane to 10 to 20 degrees (fig. S1B). In experiments using tungsten electrodes, the coil was positioned obliquely near the transverse plane superior to the visual cortex, and the angle of the electrode penetration was instead made at P4.5,L2, with an angle of

A45, M0 (fig. S1C). In all configurations, the midpoint of the coil was centered on the craniotomy in area 17 and was located between 1 and 2 cm from the skull. Pulse trains were delivered by TTL digital pulses with parametrically varying frequency (1,4,8 Hz) and duration (1,2,4 s) at 100% stimulation intensity. At this intensity and range of distances (1-2 cm distance from the skull), the induced electric field strength is estimated to be ~100-200 V/m (*2*). Given that magnetic stimulation induces an electric field which is relatively insensitive to the conductivity of the skull and protective tissues, the small (~2-4 mm) craniotomy and duratomy used in our preparation are not expected to significantly alter induced currents (*3*). In experiments that varied TMS pulse train duration and frequency, parameters were varied randomly across trials. To ensure sufficient neural recovery after each TMS trial, stimuli were displayed periodically until the evoked response maintained a steady state value for over 1 minute. A minimum of 6 minutes was provided between TMS applications, and 10-15 minute intervals were typical.

Data Acquisition:

Electrophysiology: Simultaneous oxygen and neural measurements were made using multibarrel carbon fiber microelectrodes (CARBOSTAR-7, Kation Scientific, Minneapolis, MN). These electrodes are composed of a central glass barrel containing a spark-etched carbon fiber, surrounded by 7 pipette barrels (*4*). The total tip diameter is between 10 and 20 μm, and the conical carbon tip extends roughly 15 μm beyond the glass pipette tips (*4*). The carbon fiber was used to measure tissue oxygen levels (as described below), and extracellular neural recordings were made by filling one of the surrounding barrels with 3 M NaCl (8-10 MΩ at 1KHz). Neural signals passed first through a high impedance head-stage, then through a preamplifier (Plexon,

Dallas TX). At this stage, the signal was amplified and separated into two components. The LFP signal was obtained via analog filtering of the broadband neural signal with a low-pass cutoff of 0.7 Hz and a high-pass cutoff of 170 Hz. The LFP signal was then digitized at 500 Hz. The multi-unit signal was obtained by filtering between 500 Hz and 8 MHz. From this signal, single units were discriminated online based on the temporal shapes of their extracellular potentials. Spike times were recorded with 0.04 ms precision.

Carbon fibers were converted into amperometric oxygen sensors by applying a negative polarization voltage between the carbon tip (cathode) and an external Ag/AgCl reference electrode (anode) (*5*). Amperometric oxygen sensors composed of carbon have been used previously to measure oxygen tension in various biological tissues including brain tissue (*6, 7*). Polarization between the anode and cathode, between -0.8 and -0.95 V, was set to the center of the plateau region in the current voltage curve. Within this region, the sensor current is determined by the diffusion of oxygen at the cathode and is relatively insensitive to small changes in the applied voltage. A high impedance picoammeter (Unisense**,** Denmark) provided the polarization voltage and measured the small currents generated by the sensor.

Calibration of the carbon fiber oxygen sensor was performed in a 0.9% NaCl solution. The partial pressure of oxygen in the solution was varied by bubbling a mixture of oxygen and nitrogen gas through the saline. Calibration was performed at a minimum of five levels of oxygen, and a linear relationship between current and oxygen partial pressure was observed in all electrodes tested (fig. S2A). To avoid possible deposition of biological material on the cathode surface due to long term use (*5*), a new carbon fiber sensor was used in each experiment.

While it is possible that electroactive species present in brain tissue could affect oxygen measurements, our data indicate that these contributions are minimal. We compared signals

from the carbon fiber sensor with those from a Clark-style oxygen electrode (Unisense, Denmark), which incorporates an oxygen selective membrane and guard cathode to increase the sensitivity and precision of measurements. In *in vivo* tests, both electrodes were lowered into visual cortex and were co-localized to within 100 μm. The simultaneously recorded oxygen measurements were virtually equivalent, with correlation coefficients ranging between 0.9 and 0.99 across sites.

Prior to application of TMS, stimulus evoked oxygen responses were obtained at each site. This protocol consisted of 15 to 60 repeated displays of a 4 s drifting grating, with a variable inter-stimulus interval of 24-30 s. The average evoked oxygen responses obtained at all sites were similar to those reported in previous studies (fig. S2B) (*8*).

In addition to neural-oxygen recordings with carbon fiber electrodes, we applied the same TMS protocol to two animals in which single-unit recordings were made with epoxy coated tungsten microelectrodes (5 MΩ). Tungsten electrodes were mounted in a dual array, allowing us to efficiently increase the sample size of neural data. These experiments also allowed us to confirm that the observed neural effects of TMS were independent of the type of recording electrode and the exact coil configuration (fig. S1). No qualitative differences were found between the neural responses recorded with carbon fiber electrodes and those recorded with tungsten electrodes.

Optical Imaging: In optical imaging experiments (n = 3 mature cats), the brain was stabilized with agar (1.5%) and images were obtained through a glass coverslip. The cortex was illuminated with green light (570 ± 5 nm) from two fiber-optic light guides. At this wavelength of illumination, oxygenated hemoglobin and deoxygenated hemoglobin have equal absorption

coefficents, and therefore changes in reflectance correspond to changes in the total level of hemoglobin (Hbt) (*9, 10*). The reflectance signal was captured with a Dalsa CCD camera (Dalsa INC., Ontario, Canada) using a modified macroscope (2 Nikkor, 50-mm camera lenses mounted front-to-front)(*11*). Images were stored at an effective frame rate of 6.75 Hz, using custom software written by TD.

Before applying the TMS protocol, preliminary experiments were performed to ensure an Hbt response to visual stimulation. Full-field drifting gratings at 50% contrast were displayed for 4 s with a variable inter-stimulus interval of 20-30 s. In all experiments, the average change in reflectance to 10 repetitions yielded a typical stimulus evoked hemodynamic response with a peak of ~1 to 5% (*10, 12*). The TMS protocol during optical imaging trials was identical to that during neural/oxygen trials except that no visual stimulation was presented. Initial electrophysiology experiments demonstrated that tissue oxygen exhibited similar response profiles to TMS regardless of visual stimulation (fig. S6). This was confirmed with statistical analysis of the oxygen signal showing no response difference between evoked and spontaneous time intervals (see **Statistical Analysis**). In addition, TMS was applied only at 4 or 8 Hz frequency and 2 or 4 s duration.

Data Analysis:

All data analyses were performed in MATLAB (MathWorks, Inc, Natick, MA,. USA) and C++.

Neural: All data included in analyses were free of TMS-induced electrical artifacts. This was achieved by excluding any neural data that occurred between TMS pulses or earlier than 100 ms after the last pulse (fig. S3A)

Single unit data were converted into spike rates by dividing the number of spikes in a time window by the duration of that window. Note that the evoked activity was defined in terms of the absolute spike rate (i.e., without subtraction of the pre-stimulus spontaneous firing rate). This ensured that observed changes in evoked activity were not simply artifacts of changes in spontaneous firing rates. For group effects, data were averaged together first by site (which included trials with different TMS application parameters), then over sites to remove any biases from sites with more trials. Changes in spike rate were converted into percent changes from baseline for plotting purposes.

Changes in LFP power were computed in three steps. First, the continuous LFP signal for each trial was divided into smaller 2 and 8 s segments corresponding to the stimulus and inter-stimulus intervals. Line noise at 60 Hz and 85 Hz (monitor refresh rate) was removed by subtracting the best-fit continuous sine wave from the raw signal (http://chronux.org). Second, LFP spectrograms were computed using multi-taper spectral estimation (*13, 14*). The power spectrum was estimated on a 1 s window with 5 Hz bandwidth using nine Slepian data tapers. Third, the power at each frequency and time bin was normalized by the average power for that frequency in the baseline period (40 s). Note that this conversion was specific to the type of LFP signal, i.e., stimulus-evoked LFP power was normalized by the baseline power during stimulus presentations, and spontaneous LFP power was normalized by the baseline power during inter-stimulus intervals. Therefore, modulations in power represent TMS-induced, rather than stimulus-induced changes. Modulation in LFP power was first averaged over trials within site, and site-specific responses were subsequently averaged together to obtain the population responses. LFP power changes were converted into percent changes from baseline for plotting purposes.

Oxygen: Because the precise relationship between oxygen partial pressure and sensor current can change with temperature, pressure, and the diffusion properties of the solution in which measurements are made (*5*), no attempt was made to measure oxygen tension in absolute terms. Oxygen signals were converted to a percent change from the average signal during the baseline period (40 s). To examine the population time course, trials were averaged within the same site, then over all sites.

TMS application produced transient disruptions in the tissue oxygen signal which lasted 1-3 s beyond the cessation of the pulse train (fig. S3B). These periods were excluded from all analyses of tissue oxygen. Note that this artifact prevented analysis of the early time period which could potentially include an initial dip in the oxygen response (*8*). Previous studies have demonstrated an initial negative deflection of the oxygen signal that is closely linked to local neural activity and presumably reflects an increase in oxygen consumption (*8*). In accordance with these earlier studies, our preliminary optical imaging experiments (which do not contain TMS artifacts, see **Optical Imaging**) have revealed significant increases in deoxyhemoglobin in the first 4 s post- TMS (data not shown). These data are consistent with an initial increase in oxidative metabolism due to neural activation following TMS.

Optical Imaging: Regions of interest were manually defined and typically included the full extent of exposed cortical surface. Manual delineation and an intensity threshold were used to exclude pixels corresponding to large vessels in order to target responses in the microvasculature. For each pixel, linear trend was removed and the baseline was calculated as the mean intensity of all time points preceding the TMS pulse train. The time course of each

pixel was then converted to a percent signal change by subtracting and then dividing each time point by the baseline value. Finally, to generate the mean Hbt time course, the resulting time series were averaged over all pixels, repetitions, and experiments.

Due to the nature of the optical signal, no TMS artifacts were observed. This was verified with recordings of a static, non-physiological test surface. Variations in the reflectance signal during TMS application were within noise levels of the camera (data not shown).

Statistical Analysis: Separate 3-way repeated measures ANOVAs were conducted for the spike and oxygen data. The ANOVAs included 3 factors: activity state (evoked vs. spontaneous), TMS pulse frequency (1, 4, or 8 Hz), and time (0-20 s post-TMS, 30-90 s, 180-210 s), with time as the repeated measure. Due to the limited number of trials over which pulse duration was varied, it was not incorporated as a factor. The ANOVAs included only trials with 4 s pulse duration, as they constituted the largest proportion of the data set. For oxygen data, the first time interval was 8-20 s to exclude the TMS artifact.

In post-hoc analyses of oxygen and spiking data, statistical significance was assessed by pairwise comparisons of signals before and after TMS for each trial (Wilcoxon sign rank tests). Identical tests were applied to the additional LFP and Hbt data sets. Unless otherwise noted, all *P*-values were Bonferroni corrected for multiple comparisons over time intervals.

Time-Lag Correlation Analysis: Time-lag correlations were performed between simultaneously collected neural and oxygen trials (fig. S8). A correlation analysis between spontaneous spiking activity and tissue oxygen could not be performed due to low firing rates (typically less than 1 spike/s during baseline) and the rectifying nonlinearity of spiking activity (i.e., spike rate cannot

become negative). Neural signals were shifted from -60 to +60 s in 5 s steps. Positive delays represent a shift in the neural signal forward in time (rightward) relative to the oxygen signal. Pearson's correlation coefficients were computed between the raw neural response level and the raw oxygen level averaged over a 5 s window. Correlation coefficients were converted into z-scores using Fisher's *Z*-transform, which reduces skew and approximates a normal distribution (*15*). Mean *z*-scores were reverse transformed into correlation coefficients for plotting purposes. Correlations at individual time-lags were considered positive when the mean of the *z*-score distribution was significantly larger than zero (one-tailed *t*-test). *Z*-scores at different time-lags were compared using a paired *t*-test.

Time-lag correlation curves for different neural bands were compared with regard to their magnitudes and shapes. For each curve, the correlation magnitude was estimated by averaging the *z*-scored correlation coefficient over time lags from +5 to +40 s. This time window was defined to include time delays which showed significant correlations for all neural bands. To assess differences in curve shape between neural bands, we calculated the center of mass of each curve after it was normalized from 0 to 1. This metric of correlation latency provides a robust estimate of the skew of the curve, without an implicit assumption of curve shape.

Analysis of Parametric TMS Application: Analysis of neural and oxygen changes to different levels of TMS application included all trials with appropriate stimulation parameters. Alterations in neural activity were calculated as a change in spike rate, rather than a percentage change, due to the large difference between evoked and spontaneous baselines (e.g., a change of 1 spike/s is a ~100% change in spontaneous rate, yet only a ~3% change in evoked activity).

Changes in spiking activity and tissue oxygen were calculated over identical time windows (early changes: 0 to 20 s; late changes: 30 to 90 s post-TMS).

The approximately linear relationship between neural and oxygen signals is consistent with current models of neurovascular coupling. It is also possible that components of the hemodynamic response may be due to direct action of TMS on vascular tissue. However, previous studies indicate that the excitation threshold of neural tissues is an order of magnitude less than that of other tissues, including vascular smooth muscle cells (*16-18*). In addition, application of tetrodotoxin to eliminate neural activation also abolished vascular responses to direct electrical stimulation at intensities exceeding those used here (*19*). We therefore expect that the observed hemodynamic changes are primarily of neural origin.

Phase Locking Analysis: A phase locking index was computed for trials in which we could obtain artifact-free recordings of both isolated spikes from single units and LFPs from the same electrode. This included 129 trials across 4 animals. We chose an index of phase locking that utilizes the analytic signal approach to estimate the instantaneous LFP phase at which each spike occurs (*20*). The phase locking index corresponds to one minus the circular variance of this phase distribution (*21*, *22*), which is also equivalent to the mean resultant vector strength (VS) in directional statistics (*23*). We chose this measure of phase locking because of its relative insensitivity to changes in signal amplitude. This is in contrast to alternative indices of synchrony, such as coherence (*14*), that confound changes in signal *amplitude* with changes in signal *phase* (*20*). In general, most analyses involve data characterized by amplitude changes, and this is especially true in our data set which reveals large changes in both LFP power and spike rate. In the analytic signal approach, phase information is retained while amplitude

information is discarded, so the phase locking index is derived independently from LFP amplitude. This point is true as long as the signal-to-noise ratio (SNR) of the LFP is large enough to display oscillatory behavior from which the instantaneous phase can be estimated. To check this, we verified that analyses with different SNR cutoffs yielded equivalent results. In addition, changes in spike rate might also influence this index due to statistical bias in the circular variance. This possibility is corrected for by a spike count matching procedure described below.

Data analysis proceeded as follows. After removal of line noise, the LFP trace for each TMS trial was divided into data segments that corresponded to each 2 sec stimulus presentation for evoked activity or each 8 sec ISI for spontaneous activity. These data segments were then filtered in 5 Hz bands from 1-150 Hz using the EEGLAB (*24*) function 'eegfilt'. This function utilizes the MATLAB function 'filtfilt' which preserves phase information. Instantaneous phases for these filtered segments were then extracted from the analytic signal obtained through the Hilbert transform (*20*). Each spike was then assigned the phase value with the matching time stamp.

Because the circular variance statistic is biased by the number of observations (*25*) and because TMS altered spike rate, it was necessary to take this change into account. Intuitively, this problem can be understood in the following way. Increasing the number of spikes per oscillation necessarily increases the spread in the phase distribution because some spikes must now occur at different, additional phase values. With only a small number of spikes, these additional phase values will not necessarily occur, and the variance of the phase distribution can remain small.

To correct for the change in spike rate after TMS, we used the following matching procedure. First, the spike count during each cycle of the LFP oscillation was tabulated for both pre-TMS and post-TMS intervals. Second, VS was calculated separately for each spike count by grouping cycles with matching numbers of spikes. Third, a set of ΔVS values was obtained by subtracting pre-TMS VS values from the post-TMS VS values that were matched for spike count. Fourth, the mean of these values over all spike counts yielded the final ΔVS. In order to increase the number of cycles matched for spike count, data were collapsed into 30 second periods (corresponding to 3 evoked/spontaneous intervals). This matching procedure ensured that changes in VS after TMS could not be accounted for by changes in spike rate. This procedure was applied to individual TMS trials which were then averaged to yield the population average in Figure 4C. To calculate ΔVS for gamma (20-80 Hz) and high gamma (80-150 Hz) bands in Figure 4C, values were averaged across 5 Hz frequency bands. Statistical significance was assessed using a randomization test. The pre-TMS and post-TMS phases were shuffled and ΔVS was recalculated 5000 times to generate a null distribution. The actual ΔVS value was deemed significant if it exceeded 95% ($P < 0.05$) of this null distribution after Bonferroni correction for 24 multiple comparisons (i.e., 6 LFP bands *X* 2 time intervals *X* 2 stimulus conditions). The standard errors in Figure 4C were estimated with a bootstrap procedure in which a resampled distribution of ΔVS values was constructed by resampling the phases for each time interval and 5 Hz frequency band 1000 times with replacement. The bootstrapped standard error of ΔVS for each band and time point was computed as the standard deviation of the resampled distribution. The standard errors for ΔVS in gamma and high gamma bands in Figure 4C were propagated from those of the individual 5 Hz bands across which each range was collapsed.

Spontaneous vs. Evoked Activity: Intermittent presentation of visual stimuli allowed us to examine how TMS affects both ongoing spontaneous activity and stimulus evoked activity. Our results demonstrate robust differences between activity states (Fig. 2A, fig. S5). While the detailed cellular and circuit mechanisms underlying these differences remain to be determined, we can identify several mechanisms that are likely to contribute. For instance, the immediate increase in spontaneous activity following TMS is presumably due to direct depolarization from the induced electric field (*26*). Depolarization likely originates in a distinct population of neurons (*26*) and may be amplified via recurrent synaptic excitation to generate spontaneous activity in a larger population that outlasts the period of TMS application. Indeed, previous studies using electrical stimulation have reported that single pulses elicit reverberating volleys of excitation (*27*).

In contrast to spontaneous activity, stimulus evoked activity depends on the intact function of a cortical circuit. TMS may act through several intrinsic and extrinsic factors, such as a predominance of inhibitory activation (*28*), intrinsically-mediated changes in polarization (*29*), or short term depression (*30*) to mediate disruption of this function. Support for this interpretation comes from our analysis of phase locking (Fig. 4) which demonstrates substantial desynchronization of signals between interconnected neurons. The temporal disruption of signals potentially interferes with the stimulus processing, thereby reducing the amplitude of the evoked response.

Interestingly, recent human studies have shown somewhat similar state-dependent effects (e.g., *31, 32*). In these experiments, the application of TMS is paired to a specific brain state (e.g., applied during a resting condition or, alternatively, during the execution of a cognitive

task), and the resulting effects of TMS are dependent on this pairing. This paradigm differs from the current study in that we applied TMS only during the inter-stimulus interval (i.e., spontaneous activity) and never with presentation of the visual stimulus. However, the differential effect of TMS on spontaneous vs. evoked activity observed in the current study suggests that further studies are warranted to clarify the influence of activity state on the physiological response to TMS.

Supporting Figure Legends

Figure S1. TMS coil configurations. Illustrations of TMS coil placement for different recording methods. (A) For experiments using the neural-oxygen carbon fiber electrode, the coil was positioned posterior to the visual cortex and angled 45 degrees towards the horizontal plane, which permitted an electrode penetration into area 17 at Horsley-Clarke coordinates P3.5, L2 with an angle of P45, M0. (B) During optical imaging experiments, the coil position was adjusted to create an unobstructed view for the macrolens. This involved reducing the angle between the face of the TMS coil and the coronal plane to 10 to 20 degrees. (C) In experiments using tungsten electrodes, the coil was positioned obliquely near the transverse plane superior to the visual cortex, and the angle of the electrode penetration was instead made at P4.5, L2 with an angle of A45, M0. For all coil placements, the midpoint of the coil was centered on the area 17 craniotomy and was located between 1 and 2 cm from the skull. Physiological responses were qualitatively similar across coil configurations.

Figure S2. Oxygen sensor characterization. (A) A typical calibration curve for the carbon fiber oxygen sensor. Calibrations were performed in a 0.9% NaCl solution. Oxygen partial pressure was controlled by changing the composition of an O_2/N_2 gas mixture which was continuously bubbled through the saline solution. The polarization voltage was -0.85. Data are highly linearly correlated ($r^2 = 0.998$, $P < 10^{-9}$, linear regression). (B) An example of a stimulus evoked oxygen response obtained with the carbon fiber oxygen sensor. The stimulus (green square) was a sinusoidal grating presented for 4 s. The average oxygen trace to 59 stimulus repetitions shows

an initial dip followed by a positive overshoot, typical of evoked responses (*8*). Shaded area indicates ±1 SEM.

Figure S3. Artifacts induced by TMS. (A) The oscilloscope trace of neural activity during a TMS trial (1 Hz, 4s) reveals large electrical artifacts induced by each TMS pulse. The duration of the electrical pulse produced by the coil is on the order of 1-2 μs, however saturation of amplifiers causes considerable ringing which persists for tens of milliseconds (inset, right). Although typical extracellular potentials (inset, left) can be isolated from the trace within 30 to 50 ms after the pulse, we have exercised caution by excluding data occurring between TMS pulses or earlier than 100 ms after the last pulse. These restrictions remove the possibility of pulse contamination in the neural signal. (B) Oxygen recordings made in cortical tissue (black) and just above the cortical surface (gray) show large artifacts induced by an 8 Hz, 4 s pulse train. TMS pulses transiently disrupt polarization voltage of the amperometric oxygen sensor, and sensor current takes 1-3 s to decay back to baseline (inset). To avoid artifact contamination, we limited analysis of the oxygen signal to time points more than 4 s after the last pulse. Thus, the TMS artifact period (gray box) for a 4 s pulse train is 8 s in duration.

Figure S4. Examples of TMS neural effects. (A) Demonstration of spontaneous firing beyond the duration of TMS in two cells. All spikes (both evoked and spontaneous) are displayed in histogram format (0.5 s bins) to show activity on a finer temporal scale. Stimulus presentations are marked with green boxes. Applied TMS pulse trains were 8 Hz, 4 s (left) and 4 Hz, 2 s (right). (B) Demonstration of long-lasting suppression in a single cell. Recovery of evoked activity (green) extends beyond 13 minutes. The TMS pulse train was 8 Hz, 4 s. (C)

Comparison of the last 20 spike waveforms before (left) and the first 20 waveforms after TMS (right) for the trial shown in (B). Waveforms are largely similar, indicating that the decrease in spike rate cannot be due to movement of the electrode or alterations in the shape of the waveform.

Figure S5. Population summary of TMS neural effects. (A) Scatter plots showing spiking activity before and after TMS for all cells ($n = 47$). Pre-TMS values represent the average spike rate over the baseline period (40 s), and post-TMS values represent the mean over the first 60 s after the pulse train. Spontaneous activity (left) is significantly greater after TMS ($P < 0.001$, Wilcoxon signed rank test), and evoked activity (middle) is significantly smaller ($P < 10^{-9}$, Wilcoxon signed rank test). The changes in spontaneous and evoked spiking (right) are not significantly correlated ($r = -0.04$; $P = 0.81$, linear regression). (B) TMS-induced changes in evoked (purple) and spontaneous (green) LFP power across frequency bands for all sites ($n = 42$). Intervals marked with asterisks are significantly different from baseline ($P < 0.05$, Wilcoxon signed rank test).

Figure S6. Effect of visual stimuli on TMS-induced oxygen responses.

(A) Examples of oxygen responses in the absence of visual stimuli. The temporal response, an immediate increase followed by prolonged reduction, is similar to the response elicited during experiments in which visual stimuli were presented intermittently (see Fig. 2C). (B) Average oxygen response from experiments in which visual stimuli were presented, separated into spontaneous (purple) and evoked (green) time intervals. Oxygen levels between spontaneous and

evoked states are not significantly different ($F_{111,224} = 0.0001$, $P > 0.98$, ANOVA). Oxygen data were divided into spontaneous and evoked activity states by taking the mean response during the inter-stimulus and visual stimulus intervals, then introducing a 4s offset account for the hemodynamic delay. Varying the offset from 1-5 s produced similar results.

Figure S7. Relationships between neural and oxygen data. (A) Example oxygen (left) and neural (right) data from three representative sites. (B) A supplementary data set ($n = 43$ trials) varying pulse train duration from 2 to 4 s while keeping frequency fixed at 8 Hz. Similar to the dose-dependency observed with pulse train frequency (Fig. 3A), longer pulse train durations induce larger neural and oxygen deviations. Early changes were calculated from the average signal over the first 20 s after TMS. Late changes were calculated from the average signal between 30 and 90 s post-TMS. Where error bars are not visible, the error was smaller than the plot symbol.

Figure S8. Example of time-lag correlation between neural and oxygen data.

(A) For each trial of simultaneously collected oxygen (top) and neural data (bottom), oxygen and neural signals were correlated at a series of time delays. In this example, levels of oxygen are correlated with the stimulus evoked spike rate. Neural signals were shifted from -60 to +60 s, in 5 s steps. By convention, positive delays represent shifting the neural signal forward in time (rightward), relative to the oxygen signal. For a single time point on the neural trace (dotted line), a negative shift of -10 s (blue) and a positive shift of +10 s (red) are illustrated. (B) Scatter plots of all the neural and oxygen data points at a time shift of -10 s (left) and +10 s (right). Correlation coefficients at these time delays are $r = 0.46$ and $r = 0.70$, respectively. Dashed lines

indicate the least-squares regression line. (C) A plot of correlation coefficients at all time delays (from -60 to +60 s). The curve is weighted toward positive time delays, suggesting that the oxygen signal lags behind the neural signal.

Figure S9. Increased perfusion does not affect TMS-induced neural suppression.

(A) Tissue oxygen during a TMS trial in which mild hypercapnia (5% CO_2 for 4.5 min, yellow shading) was induced to manipulate oxygen levels. Hypercapnia causes vasodilation and thus increases the partial pressure of oxygen within the tissue. When TMS is applied during hypercapnia, the level of tissue oxygen remains above initial baseline levels, even during the extended decrease (red arrow). (B) Neural suppression caused by TMS occurs even in the presence of elevated levels of tissue oxygen. Note also that the neural response continues to recover following the cessation of hypercapnia, despite an overcompensation effect in the tissue oxygen which drives it below the pre-hypercapnia baseline. This implies that hypoxia is not the basis of the TMS-induced neural suppression. (C) End-tidal CO_2 during the hypercapnic modulation. The maximum level of expired CO_2 was 56 mmHg.

Figure S1

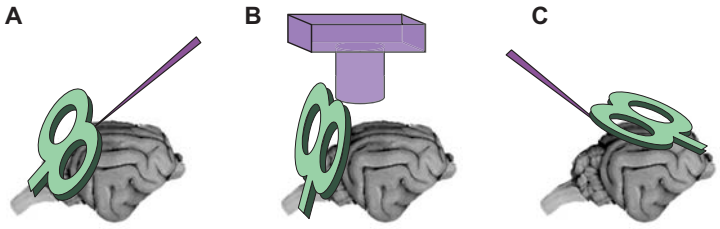

Figure S2

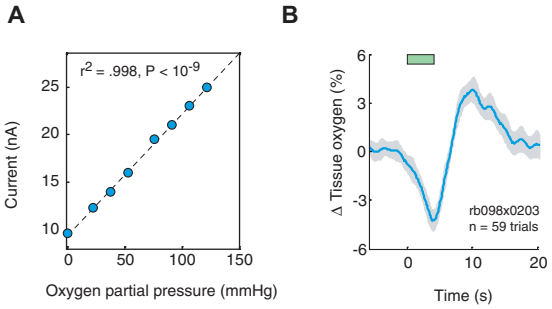

Figure S3

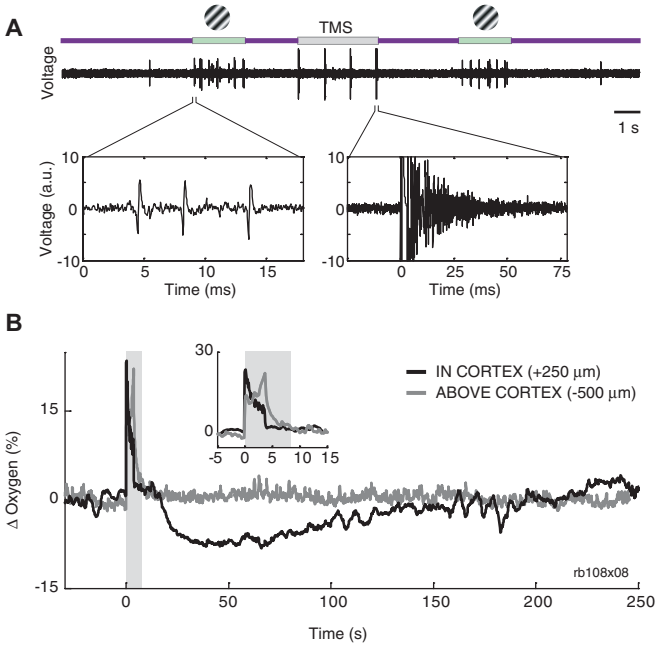

Figure S4

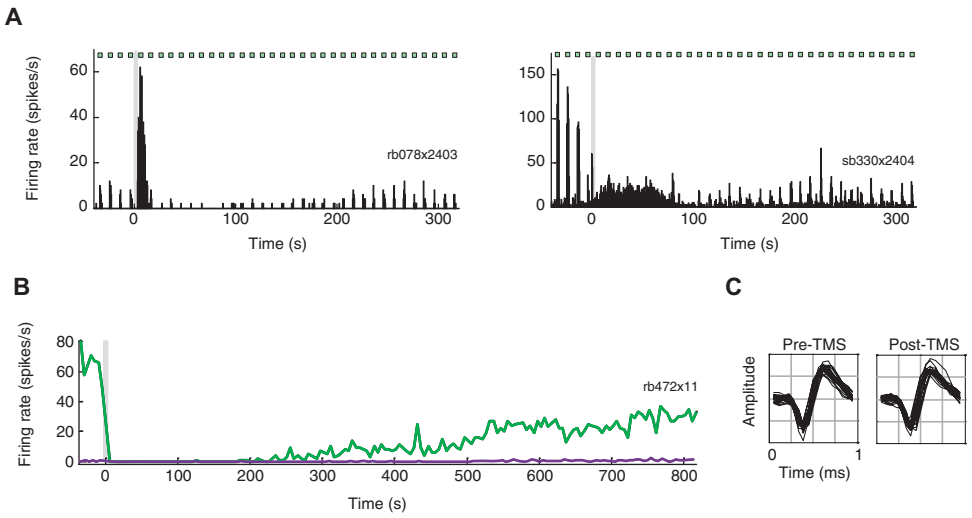

Figure S5

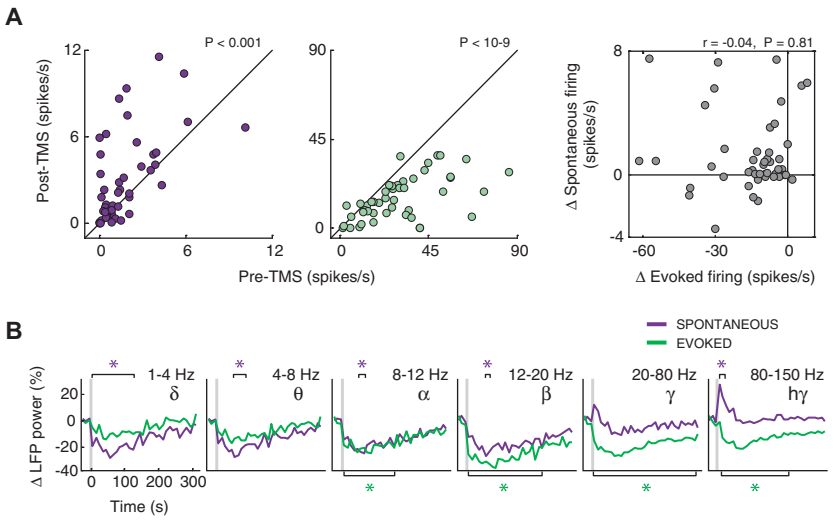

Figure S6

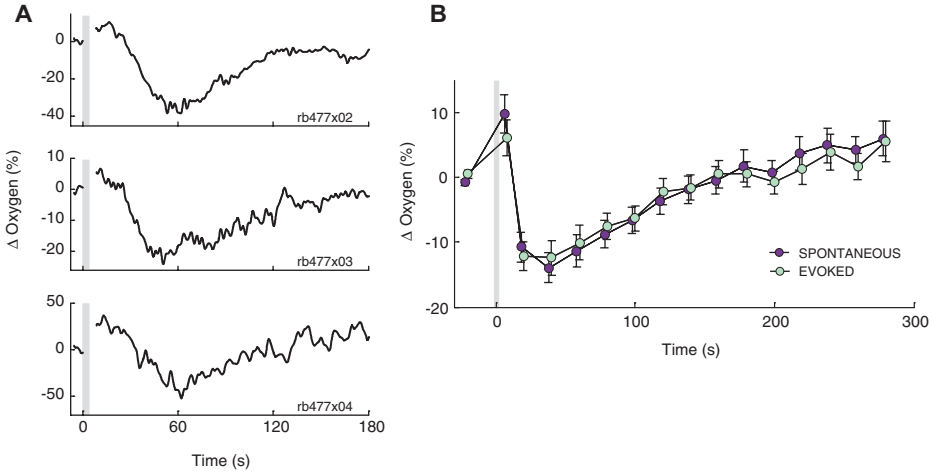

Figure S7

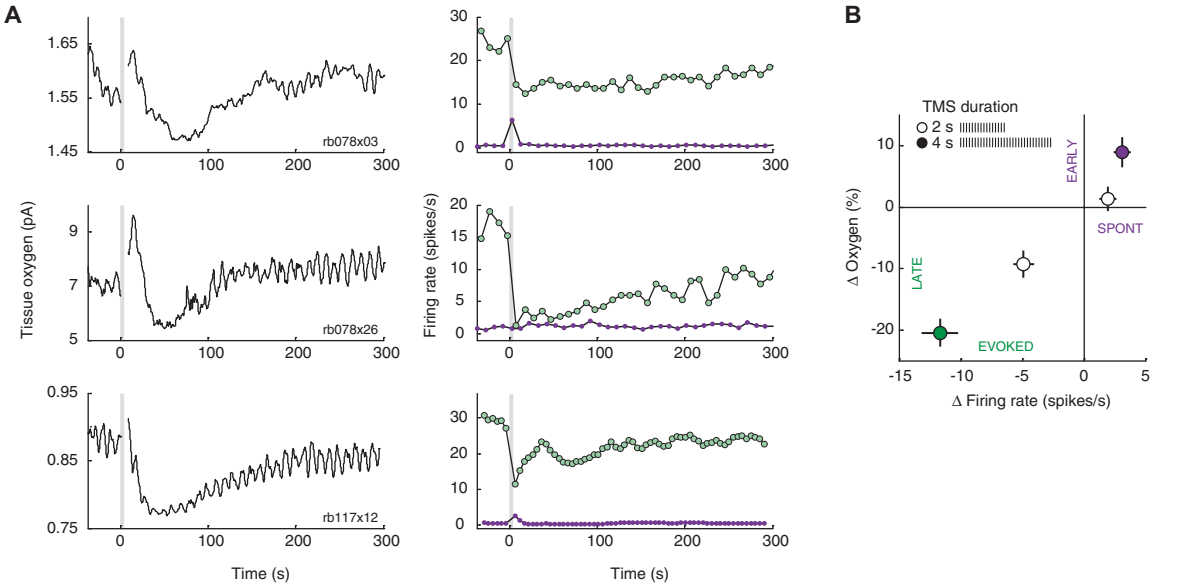

Figure S8

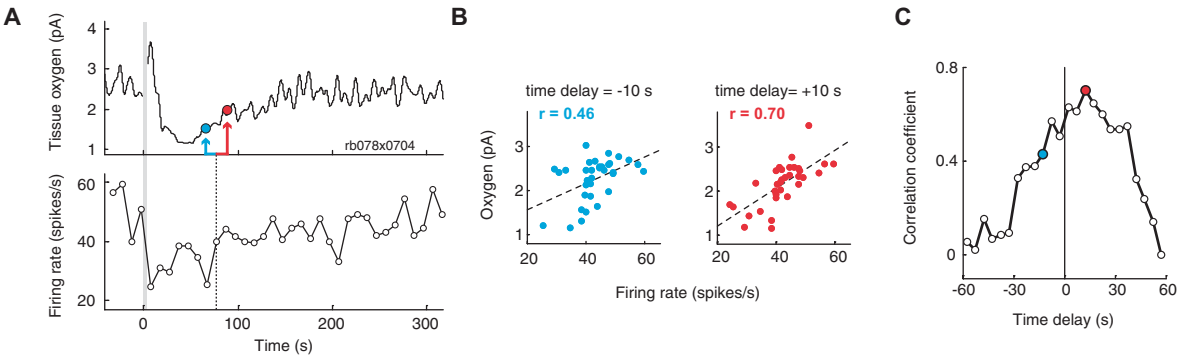

Figure S9

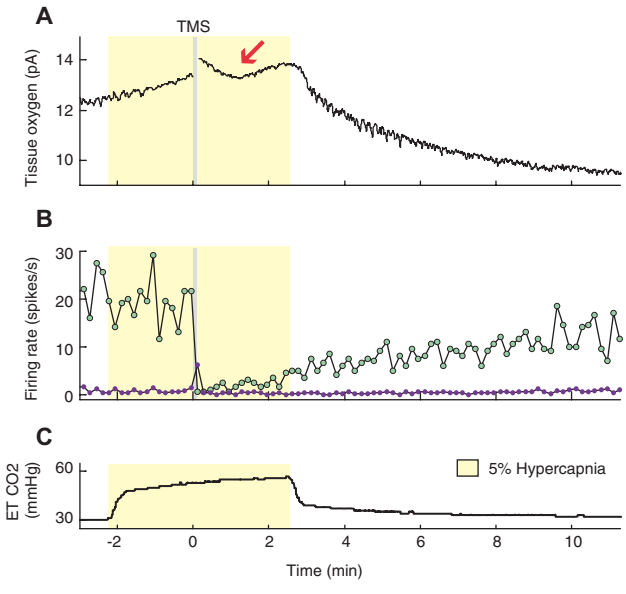

Supporting References and Notes

1. V. Horsley, R. Clarke, *Brain* **31**, 45 (1908).
2. F. S. Salinas, J. L. Lancaster, P. T. Fox, *Phys Med Biol* **52**, 2879 (2007).
3. B. J. Roth, J. M. Saypol, M. Hallett, L. G. Cohen, *Electroencephalogr Clin Neurophysiol* **81**, 47 (1991).
4. D. Budai, Z. Molnar, *Acta Biologica Szegediensis* **45**, 65 (2001).
5. I. Fatt, *Polagraphic Oxygen Sensors* (CRC, Cleveland, OH, 1976), pp.
6. L. C. Clark, Jr., E. W. Clark, *Ala J Med Sci* **18**, 142 (1964).
7. L. C. Clark, Jr., C. Lyons, *Ala J Med Sci* **2**, 353 (1965).
8. J. K. Thompson, M. R. Peterson, R. D. Freeman, *Science* **299**, 1070 (2003).
9. A. Grinvald, E. Lieke, R. D. Frostig, C. D. Gilbert, T. N. Wiesel, *Nature* **324**, 361 (1986).
10. D. Malonek, A. Grinvald, *Science* **272**, 551 (1996).
11. A. Grinvald, R. D. Frostig, E. Lieke, R. Hildesheim, *Physiol Rev* **68**, 1285 (1988).
12. D. Malonek *et al.*, *Proc Natl Acad Sci U S A* **94**, 14826 (1997).
13. D. J. Thomson, *Proceedings of the IEEE* **70**, 1055 (1982).
14. B. Pesaran, J. S. Pezaris, M. Sahani, P. P. Mitra, R. A. Andersen, *Nat Neurosci* **5**, 805 (2002).
15. C. Olson, *Statistics: Making Sense of Data.* (Allyn and Bacon, Newton, MA, 1987), pp.
16. F. Girling, *Am J Physiol* **170**, 131 (1952).
17. R. M. Rapoport, J. A. Bevan, *J Pharmacol Exp Ther* **218**, 375 (1981).
18. G. N. Sibley, *J Physiol* **354**, 431 (1984).
19. N. Akgoren, P. Dalgaard, M. Lauritzen, *Brain Res* **710**, 204 (1996).
20. M. Le Van Quyen *et al.*, *J Neurosci Methods* **111**, 83 (2001).
21. H. Lee, G. V. Simpson, N. K. Logothetis, G. Rainer, *Neuron* **45**, 147 (2005).
22. J. Jacobs, M. J. Kahana, A. D. Ekstrom, I. Fried, *J Neurosci* **27**, 3839 (2007).
23. K. V. Mardia, P. E. Jupp, *Directional statistics* (John Wiley and Sons, New York, 2000), pp.
24. A. Delorme, S. Makeig, *J Neurosci Methods* **134**, 9 (2004).
25. Y. Ben-Shaul *et al.*, *J Neurophysiol* **89**, 1136 (2003).
26. S. H. Lisanby, R. H. Belmaker, *Depress Anxiety* **12**, 178 (2000).
27. H. D. Patton, V. E. Amassian, *J Neurophysiol* **17**, 345 (1954).
28. A. Hiller *et al.*, *J Neurosci Methods* **159**, 286 (2007).
29. M. V. Sanchez-Vives, L. G. Nowak, D. A. McCormick, *J Neurosci* **20**, 4267 (2000).
30. Y. Schiller, Y. Bankirer, *J Neurophysiol* **97**, 1887 (2007).
31. A. T. Sack *et al.*, *Cereb Cortex* (2007).
32. B. Fierro *et al.*, *J Physiol* **565**, 659 (2005).